Open Research Online

Evolution of prolate molecular clouds at H II boundaries - II. Formation of BRCs of asymmetrical morphology

Journal Item

For guidance on citations see FAQs.

Version: Version of Record

oro.open.ac.uk

Evolution of prolate molecular clouds at H II boundaries – II. Formation of BRCs of asymmetrical morphology

T. M. Kinnear,[1]⋆ J. Miao,[1] G. J. White,[2,3] K. Sugitani[4] and S. Goodwin[5]

[1]*Centre for Astrophysics and Planetary Science, School of Physical Sciences, University of Kent, Canterbury CT2 7NH, UK*
[2]*Department of Physics and Astronomy, The Open University, Milton Keynes MK7 6AA, UK*
[3]*Space Science and Technology Department, CCLRC Rutherford Appleton Laboratory, Oxfordshire OX11 0QX, UK*
[4]*Graduate School of Natural Sciences, Nagoya City University, Mizuho-ku, Nagoya 467-8501, Japan*
[5]*Department of Physics and Astronomy, The University of Sheffield, Western Bank, Sheffield S10 2TN, UK*

ABSTRACT

A systematic investigation on the evolution of a prolate cloud at an H II boundary is conducted using smoothed particle hydrodynamics in order to understand the mechanism for a variety of irregular morphological structures found at the boundaries of various H II regions. The prolate molecular clouds in this investigation are set with their semimajor axes at inclinations between $0°$ and $90°$ to a plane-parallel ionizing radiation flux. A set of four parameters, the number density n, the ratio of major to minor axis γ, the inclination angle φ and the incident flux F_{EUV}, are used to define the initial state of the simulated clouds. The dependence of the evolution of a prolate cloud under radiation-driven implosion (RDI) on each of the four parameters is investigated. It is found that (i) in addition to the well-studied standard type A, B or C bright-rimmed clouds (BRCs), many other types such as asymmetrical BRCs, filamentary structures and irregular horse-head structures could also be developed at H II boundaries with only simple initial conditions; (ii) the final morphological structures are very sensitive to the four initial parameters, especially to the initial density and the inclination; (iii) the previously defined ionizing radiation penetration depth can still be used as a good indicator of the final morphology. Based on the simulation results, the formation time-scales and masses of the early RDI-triggered star formation from clouds of different initial conditions are also estimated. Finally a unified mechanism for the various morphological structures found in many different H II boundaries is suggested.

Key words: hydrodynamics – radiative transfer – stars: formation – ISM: evolution – H II regions – ISM: kinematics and dynamics.

1 INTRODUCTION

As the intensive Extreme Ultraviolet (EUV) radiation from newly formed star(s) ionizes the star-facing surface layer of a molecular cloud, the ionization heating induces a shock which propagates into the cloud, compressing material to form highly condensed core(s). These cores are the potential sites for EUV radiation triggered new star formation. Simultaneously the Hα emission produced by the recombination of ions with electrons creates a bright rim around the star-facing side of the cloud. The structures formed are termed bright-rimmed clouds (BRCs), the best candidate for studying the feedback of massive stars to surrounding and parental molecular cloud(s). This process is the radiation-driven implosion

(RDI) mechanism for EUV radiation triggered star formation in BRCs.

Multiwavelength observations have revealed various physical and morphological properties of BRCs at H II regions. BRCs observed so far tend to be classified as type A, B and C in increasing order of the curvature of their bright rim (Sugitani, Fukui & Ogura 1991; Sugitani & Ogura 1994), though some of BRCs are found in M-shaped morphology (Osterbrock 1957; Karr, Noriega-Crespo & Martin 2005; Urquhart et al. 2006).

Starting with a uniform and spherical molecular cloud illuminated by a plane-parallel ionizing radiation from one side, theoretical modelling based on the RDI mechanism successfully revealed the formation process of standard type A, B or C BRCs. These simulated BRCs are all symmetric to their structure axis, and the latter aligns with the radiation flux direction, i.e. the line connecting the tip of a BRC and the centre of the exciting star (Bertoldi 1989; Lefloch & Lazareff 1994; Kessel-Deynet & Burkert 2003; Miao et al. 2006,
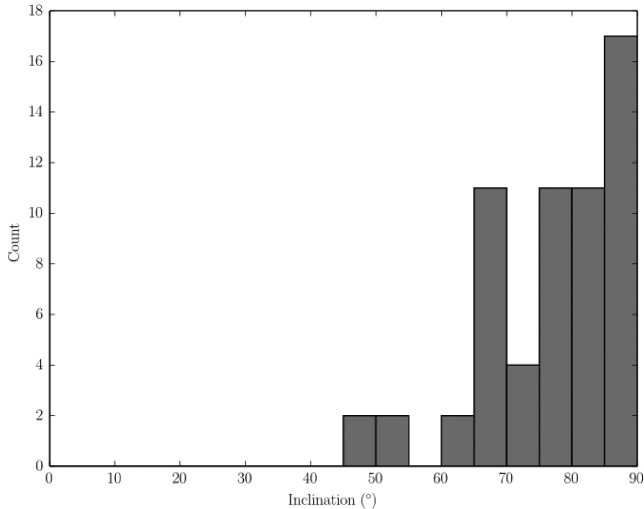
Figure 1. The distribution of the inclination angle φ, which is defined as the angle between the major axis and the *x*-axis as shown in Fig. 2, of the BRCs in about 10 emission nebulae (Osterbrock 1957).

Figure 2. The initial geometry of a prolate cloud in simulations. x_p, x_a and x_{max} are the *x*-projections of the apex, the semimajor axis a and the farthest point of the cloud from *z*-axis, respectively.

2009, 2010; Gritschneder et al. 2009; Bisbas et al. 2011; Haworth & Harries 2012; Tremblin et al. 2012).

However, further investigation on the observed structures at H II boundaries finds that (i) some BRCs do not show a comet-like morphology, but fragment-core linear structures perpendicular to the EUV radiation flux direction (e.g. Chauhan et al. 2011); (ii) most type A, B and C BRCs are not symmetric about their structural axes, which also do not necessarily align with the radiation flux direction of their exciting stars (Morgan et al. 2004; Thompson, Urquhart & White 2004). As shown in Fig. 1, there is a distribution in the angle between the axis of a BRC and the direction from the tip of the BRC to the centre of the exciting star, based on the observational data on groups of BRCs in about 10 emission nebulae (Osterbrock 1957); (iii) there are more objects with structures which cannot be categorized by type A, B or C than those which can be; (iv) in those asymmetrical BRC structures, RDI-triggered multistar or sequential formation are often found not only at the head of BRCs, but also in the more compressed side layer (Fukuda et al. 2013; Mäkelä & Haikala 2013; Panwar et al. 2014; Sicilia-Aguilar et al. 2014). It is obvious that it is difficult to accommodate the variety of structural and physical features observed with RDI modelling starting with a spherical cloud.

Observations on the physical properties of molecular clouds have revealed that spherical clouds are very rare cases (Gammie et al. 2003; Doty et al. 2005; Rathborne et al. 2009) and there are many physical processes which lead to formation of prolate molecular clouds (Gong & Ostriker 2011; Gholipour & Nejad-Asghar 2013). To investigate the mechanism for the development of structures of various morphologies other than standard (i.e. symmetrical) BRCs at H II boundaries, using an initially non-spherical cloud, such as a prolate cloud, in RDI modelling seems the most feasible choice. Definition in terms of two additional, geometric, parameters are introduced: the ratio of the major (a) to minor (b) axis $\gamma = \frac{a}{b}$ and the inclination angle φ, the configuration of which is illustrated in Fig. 2. In this way we can expect that the variety of the morphological structures derived from RDI simulations must be greatly increased.

A set of RDI simulations were conducted using an initially prolate cloud with $\varphi = 0°$, which we call 'perpendicular' to the EUV radiation flux. It is found that a perpendicular prolate cloud would evolve into a perpendicular fragment-core linear structure to the
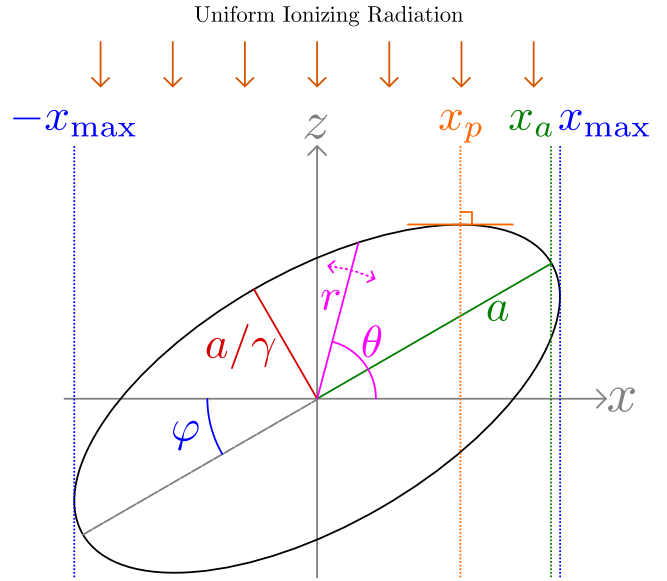
ionizing flux, covered by a bright top layer on the star side. Both the initial physical/geometrical conditions of the cloud and the strength of radiation flux affect the distribution of condensed cores over the structure, the total condensed core mass and the triggered star formation time. The sporadic fragment-core structures at H II boundaries can be interpreted by the effect of the interaction between a perpendicular prolate cloud and a parallel-plane EUV radiation field. More details are presented in Kinnear et al. (2014).

In this paper, we expand the investigation to the evolution of a prolate cloud at H II boundaries, with the cloud's major axis inclined to the EUV radiation flux by an angle $0° \leq (90° - \varphi) \leq 90°$. This is performed in order to understand the mechanism for the formation of a broad range of asymmetrical structures and the consequent triggered star formation inside them. In the rest of the paper, we first present a brief description of the codes used, the initial conditions of the clouds for simulations, and a derived quantity which gives an indication of the dynamic evolution of prolate clouds at different H II boundaries. In the results and discussion section we present simulation results and discuss the physical mechanism responsible for the formation of different morphological structures at H II boundaries. Finally, conclusions are drawn.

2 THE CODES AND INITIAL CONDITIONS

2.1 The codes

An updated smoothed particles hydrodynamics (SPH) CODE II is used for all of the simulations investigated in this paper, which is an extended version of CODE I (Nelson & Langer 1999). CODE I is an SPH code to investigate the effect of an isotropic FUV interstellar background radiation on the evolution of a molecular cloud, by solving the full set of hydrodynamic equations, including self-gravity of the cloud and a chain of chemical differential equations. Based on CODE I, a numerical solver with a ray-tracing algorithm (Kessel-Deynet & Burkert 2000) for a plane-parallel EUV radiation transferring equation was implemented, as well as the relevant heating and cooling processes. We refer to this version as CODE II,

which can be used to investigate the interaction of a plane-parallel ionizing radiation from massive star(s) with a molecular cloud of arbitrary initial geometry. More detailed descriptions of the code can be found in Miao et al. (2006) and Kinnear et al. (2014).

By virtue of the asymmetric morphology of the simulated clouds, the condensed cores triggered by RDI-induced shocks are not usually aligned with the structural axis and multistar formation is also frequently observed. To identity the positions of these triggered condensed cores and analyse their physical properties, a code called 'COREFINDER' is used, for which a detailed description is included in Kinnear et al. (2014). For the simulations presented in this paper, all 'cores' are defined as a region of at least 0.03 $M_{\odot}$ (>100 SPH particles) and the density of each SPH particle sampled must be $n \geq 10^6$ cm^{-3}. As in Kinnear et al. (2014), the cores formed from the simulations are the first generation of RDI-triggered objects. Simulations for the subsequent generations of RDI-triggered star formation becomes excessively slower after initial extremely high density core(s) form, which leads to a decrease towards infinitesimally small time steps, and the effective halt of the simulation. This can be avoided by the use of the 'sink' particles of Bate & Burkert (1997), but is not currently implemented in CODE II. As such, the cores formed here will be termed 'early' generation triggered cores, and represent the earliest batch of triggered objects.

All of the column density images are produced using the software SPLASH, which is specially designed for processing SPH numerical data (Price 2007).

2.2 Initial conditions

2.2.1 Initial geometry

The geometrical shape of a prolate cloud in the simulations is described by a pair of initial parameters (a, γ) and its orientation to the plane-parallel ionization radiation flux is $0° \leq \varphi \leq 90°$, as shown in Fig. 2. The ionization flux on to the surface of the cloud on the star side is treated as plane-parallel to the z-axis, for an assumed large ratio of distance to the illuminating star against cloud size.

In Fig. 2, x_p is the x-coordinate of the apex of the cloud. Letting r be the distance of any point on the surface of a prolate cloud in the xz plane, and θ the angle between r and the x-axis, we have,

$$r = \frac{a}{\sqrt{\cos^2(\theta - \varphi) + \gamma^2 \sin^2(\theta - \varphi)}}. \tag{1}$$

The maximum x-coordinate and the x-projection of the semimajor axis

$$x_{\max} = a \sqrt{\cos^2 \varphi + \frac{\sin^2 \varphi}{\gamma^2}}, \tag{2}$$

$$x_a = a \cos \varphi. \tag{3}$$

As an important indicator to the dynamical evolution of a prolate cloud with an inclination angle φ, the effective illuminated area by the EUV radiation is,

$$A = \frac{\pi a x_{\max}}{\gamma} = \frac{\pi a^2}{\gamma} \sqrt{\cos^2 \varphi + \frac{\sin^2 \varphi}{\gamma^2}}, \tag{4}$$

which is a decreasing function with φ, has the maximum πab at $\varphi = 0°$ and the minimum πb^2 at $\varphi = 90°$. For the convenience of the following discussion, we call the half-cloud with $\varphi \leq \theta \leq \pi + \varphi$ as the 'front' semi-ellipsoid, and $\pi + \varphi < \theta \leq 2\pi + \varphi$ the 'back' semi-ellipsoid.

2.2.2 Initial mass distribution

As we have done in the investigation of the evolution of a perpendicular prolate cloud at an H II boundary (Kinnear et al. 2014), all of the molecular clouds in our simulations start with a uniform density, which is rendered by a glass-like distribution of SPH particles created using GADGET-2 (Springel 2005). A glass-like distribution is taken as a good approximation to a uniform mass distribution. We choose the initial mass of the cloud to be 30 $M_{\odot}$, the same as used for Kinnear et al. (2014). The number of SPH particles for each molecular cloud is determined by the mass resolution, 3.0×10^{-4} $M_{\odot}$ per SPH particle, for 100 000 particles, higher than required by the convergence test of the CODE II. A zero initial velocity field is set for all of the molecular clouds in the simulations.

Since the objective of our investigation is to explore the evolution of the RDI-triggered collapse of an initially inclined prolate cloud, any initially unstable cloud against the self-gravity before interacting with the ionization radiation flux cannot be chosen. Stability is assured by applying the Jeans criteria for an isolated prolate cloud, in terms of Jeans number J, the ratio of the initial gravitational energy of a prolate cloud to the thermal energy and can be expressed as (Bastien 1983),

$$J = \frac{\pi G \rho \mu b^2}{15 e R_g T} \ln\left(\frac{1+e}{1-e}\right) \leq 1.0, \tag{5}$$

where ρ, T and μ are the mass density, the initial temperature and the mean molecular mass of the prolate cloud, respectively; G and R_g are the standard physical constants and the eccentricity,

$$e = \sqrt{1 - \frac{b^2}{a^2}} = \frac{\sqrt{\gamma^2 - 1}}{\gamma}. \tag{6}$$

Using the relation between density, mass M and volume of a cloud, we can derive the condition for the major axis a of an initially stable prolate cloud,

$$a \geq a_{\mathrm{crit}} = 0.052 \frac{M^* \gamma}{T \sqrt{\gamma^2 - 1}} \ln\left(\frac{\gamma + \sqrt{\gamma^2 - 1}}{\gamma - \sqrt{\gamma^2 - 1}}\right), \tag{7}$$

where M^* is the mass of the prolate cloud in units of solar masses, and a and a_{crit} have units of parsecs. For a given molecular cloud of mass M^*, and initial temperature T and γ, a minimum value of a can be estimated; the major axis of an initially gravitationally stable cloud should satisfy $a > a_{\mathrm{crit}}$.

2.3 Boundary condition

The clouds in our simulations are subject to an isotropic interstellar background FUV radiation of one Habing unit (Habing 1968) and an ionizing EUV radiation with a flux of 10^9 cm^{-2} s^{-1} (typical of the boundary of an H II region) directed parallel to the z-axis (along the negative z-direction) as illustrated in Fig. 2.

A constant pressure boundary condition is applied with the value of the external pressure being set equivalent to an external medium of atomic hydrogen of $n(\mathrm{H\,I}) = 10$ cm^{-3} and temperature of 100 K. An outflow condition is imposed at a fixed boundary which is a few times of the initial size of the cloud (Nelson & Langer 1999).

2.4 The ionization penetration depth parameter

In order to classify the initial dynamic regime of a perpendicular prolate cloud ($\varphi = 0$), a dimensionless parameter, d_{EUV}, was defined, being the ratio between the physical ionizing radiation penetration depth to the semiminor axis of the cloud. For this scenario,

Table 1. Summary of the test series conducted. n is initial density, γ the axial ratio, φ the inclination angle and F_0 the incident flux.

Series name	n (cm^{-3})	γ	φ (°)	F_0 ($\times 10^9$ cm^{-2} s^{-1})
G1200	1200	1–10	0–90	1
Density & flux	100–1200	2	60	1 & 2
Irregular	400	2–3.5	60–85	2

$d_{EUV} = \frac{F_{EUV}\,\gamma}{\alpha_B\,a\,n^2}$ (Kinnear et al. 2014). When $\varphi \neq 0°$, we modify its definition to the ratio of the physical ionization penetration depth to the characteristic depth of the cloud. This characteristic depth is defined as half of the longest path through the cloud in the direction of the radiation, which is always the depth of the cloud at $x = 0$, $y = 0$.

$$d_{EUV} = \frac{F_{EUV}}{\alpha_B n^2} \frac{1}{r(\theta = 90°)}$$

$$= \frac{F_{EUV}\,\gamma}{\alpha_B\,n^2\,a} \sqrt{\frac{\sin^2\varphi}{\gamma^2} + \cos^2\varphi}$$

$$= 1.6 \times 10^3 \frac{F^*_{EUV}\,\gamma}{n^2\,a^*} \sqrt{\frac{\sin^2\varphi}{\gamma^2} + \cos^2\varphi} \quad \text{(pc)}, \tag{8}$$

where the major axis a^* is in the unit of pc, and F^*_{EUV} is the EUV ionizing radiation flux in units of 10^9 cm^{-2} s^{-1}, α_B is the recombination coefficient of hydrogen ion–electron under the 'on-the-spot' approximation (Dyson & Williams 1997) and has the value of 2.0×10^{-13} cm^3 s^{-1} at a temperature of about 10^4 K (Dyson & Williams 1997). This is then taken as a constant, as the equilibrium temperature for ionized material is $\approx 10^4$ K and the dependence of α_B on temperature is not strong in the region around that temperature.

As already discussed in Kinnear et al. (2014), when $d_{EUV} \ll 1$ for $\varphi = 0$, the prolate cloud is in the RDI-triggered shock dominant region, and the collapse of the cloud is by 'foci convergence' mode, i.e. two high-density cores form at the two ends of a filament; when $d_{EUV} \leq 1$, the cloud can still be RDI triggered to collapse but through 'linear convergence', i.e. a few high-density cores form along the whole filament; when $d_{EUV} \geq 1$, the cloud is in photoionization dominant region, and would be photoevaporated. As d_{EUV} can possess a similar range of values for all φ in equation (8), we would expect it to play a similar role for $\varphi \neq 0$.

3 RESULTS AND DISCUSSIONS

Three sets of simulations were conducted using prolate clouds of different geometrical shapes (γ), inclination angles (φ), initial densities (n) and ionizing fluxes (F_{EUV}) to investigate the effect of their variations on the evolution of a prolate cloud. Table 1 contains a summary of the ranges of properties for each set. All of the clouds have an initial temperature of 60 K and are illuminated by a 50 000 K star providing a flux at the cloud, $F_0 = 10^9$ cm^{-2} s^{-1} (or 2.0×10^9 cm^{-2} s^{-1}, when specified), the same as that for Kinnear et al. (2014). In this section, we first describe the evolution of a prolate cloud of an inclination angle of 45° in detail, then investigate the influence of changing initial inclination angle φ on the evolution of the same cloud. Next we discuss how the initial geometry of a prolate cloud affects the morphological evolution of a cloud and RDI-triggered star formation inside it. Finally we propose a formation mechanism for the variety in morphological structures found at H II boundaries.

Table 2. Parameters of molecular clouds of G1200 series with an inclination angle $\varphi = 45°$. From left to right, columns 1–3 are the number identity, axial ratio and the critical semimajor axis defined by equation (7). Columns 4 and 5 are the major axis and d_{EUV} defined by equation (8). All of the semimajor axes and critical semimajor axes are in units of pc and the penetration depth is in per cent.

		G1200		
No.	γ	a_{crit} (pc)	a_{1200} (pc)	d_{EUV} (per cent)
1	1.00	0.052	0.494	0.225
2	1.25	0.060	0.573	0.218
3	1.50	0.067	0.648	0.219
4	1.75	0.073	0.718	0.221
5	2.00	0.079	0.784	0.224
6	2.25	0.084	0.849	0.228
7	2.50	0.039	0.910	0.232
8	2.75	0.093	0.970	0.237
9	3.00	0.097	1.028	0.241
10	3.25	0.101	1.084	0.246
11	3.50	0.104	1.139	0.250
12	3.75	0.107	1.193	0.256
13	4.00	0.110	1.245	0.260
14	4.50	0.116	1.347	0.268
15	5.00	0.121	1.445	0.277
16	5.50	0.126	1.540	0.285
17	6.00	0.130	1.632	0.292
18	7.00	0.138	1.808	0.307
19	8.00	0.145	1.977	0.320

3.1 Evolution of cloud G1200(5) with $\varphi = 45°$

Table 2 lists all of the relevant parameters of clouds with initial density 1200 cm^{-3} and inclination angle $\varphi = 45°$, for variations of the initial ratio γ. The cloud is the fifth one in the G1200 set, notated G1200(5). It has an initial shape defined by $\gamma = 2.0$, its major axis (0.784 pc) is ≈ 10 times of its critical major axis (0.079 pc) derived by using equation (7), indicating its initial stability against gravitational collapse.

Fig. 3 shows an evolutionary sequence of column density of the cloud over a period of 0.13 Myr. We also plot the corresponding mean axial density distribution along the x-axis in Fig. 4, with the established binning method for describing axial profiles of SPH particle properties (Nelson & Papaloizou 1993; Nelson & Langer 1999; Kinnear et al. 2014). This view provides a qualitative picture of the location of condensed cores formed in the shocked layer of gas in the cloud by the RDI effect.

It is seen from the above two figures that 28 kyr after the radiation flux was switched on, a shock is established by the ionization heating. This shock starts compressing the cloud surface on the star-facing side. A slightly compressed thin layer of mean density $\approx 3.0 \times 10^3$ cm^{-3} appears at the EUV exposed surface, as shown in the upper-middle panels in Figs 3 and 4. The density at $x = 0.49$ pc is slightly higher than the axial mean density, which reflects the very early stage of a condensed core formation around the apex of the cloud.

From $t = 0.028$ to 0.11 Myr, the shock continues propagating into the cloud. The density in the thin shocked layer continues increasing and the structure of the head becomes more distinctive. The non-head mean axial density and the central density of the head increase to 10^4 and 10^5 cm^{-3}, respectively, at 0.054 Myr, and to 2.0×10^4 and 10^6 cm^{-3}, respectively, at 0.08 Myr. At $t = 0.11$ Myr, the density in the shocked layer increases dramatically towards the apex of the
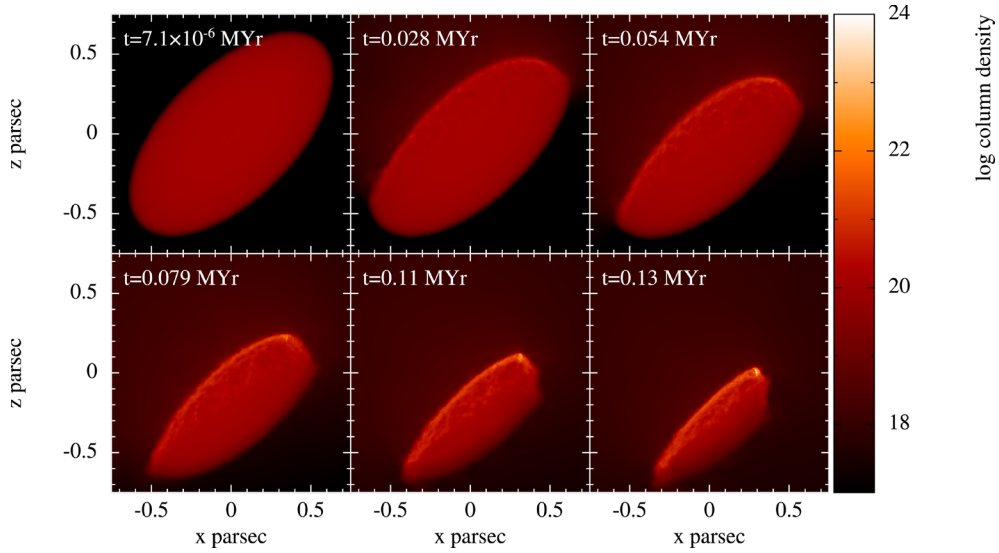
Figure 3. Sequential evolution of the column number density for cloud G1200(5) with the inclination angle $\varphi = 45°$. Time sequence is left to right, then top to bottom and then left to right.
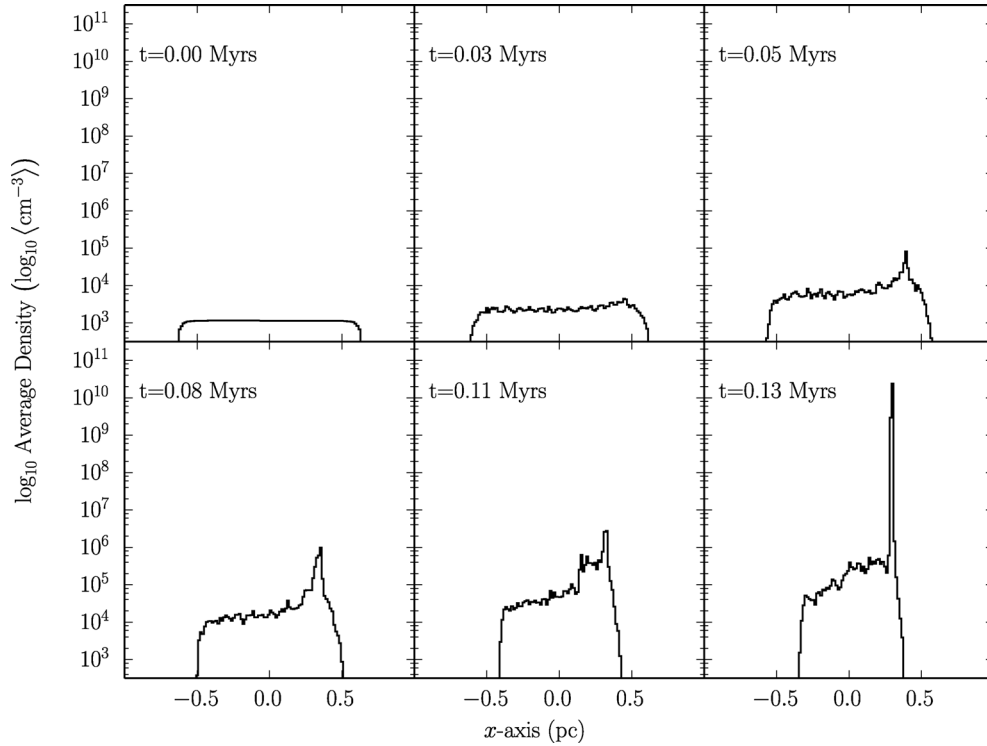

Figure 4. Axial mean density distribution along the x-axis of the cloud G1200(5) corresponding to the column density evolutionary snapshots in Fig. 3.

cloud (at $x = 0.32$ pc). This density jumps from $\approx 8 \times 10^4$ to 8×10^5 cm^{-3} at $x = 0.24$ pc, then to the maximum 4×10^6 cm^{-3} at the apex. It is interesting to find from the magnified image in the left-hand panel of Fig. 5 that a filament structure forms at the head, aligning with the EUV radiation direction. The structure has a length of roughly 0.03 pc and the top end of it coincides with the apex of the cloud.

The gas contained in both the shocked surface layer and in the filament becomes further compressed by $t = 0.13$ Myr. At this stage the mean density in the shocked layer and in the filament are 10^5–10^6 and $> 10^9$ cm^{-3}, respectively. The right-hand panel of Fig. 5

further reveals the formation of two high-density cores in close proximity. These dual cores may be the result of fragmentation of the filament-like structure observed at $t = 0.11$ Myr.

Overall, the cloud G1200(5) with an initial inclination angle of 45° evolves to an asymmetrical type B BRC, with double RDI-triggered high-density cores embedded at its head, very close to the apex of the BRC. The cores are the potential sites for new star formation. At the same time the apex of the cloud moves down from $z = 0.61$ to 0.035 pc, a net recoil velocity of $\langle v_z \rangle = 4.3$ km s^{-1}, due to the rocket effect caused by the evaporating gas from the star-facing surface irradiated by the ionizing radiation (Oort & Spitzer
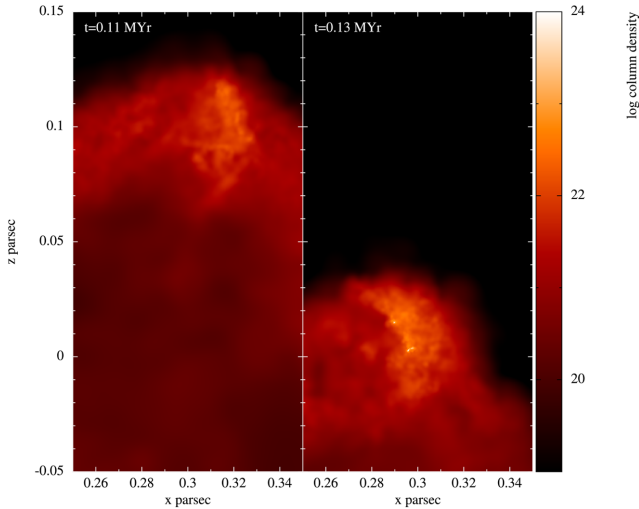
Figure 5. Magnification of the column density profiles time $t = 0.11$ (left) and 0.13 Myr (right) at the head of the cloud G1200(5) with $\varphi = 45°$.

Table 3. Variation of d_{EUV} over different φ for cloud G1200(5).

$\varphi(°)$	0	15	30	45	60	75	90
d_{EUV} (per cent)	0.283	0.276	0.255	0.224	0.187	0.155	0.141

1955). Next we investigate the effect of the inclination of a prolate cloud on its dynamical evolution.

3.2 Evolution of G1200(5) with $0° \leq \varphi \leq 90°$

To investigate the dependence on the inclination, the cloud G1200(5) is simulated for a range of inclinations $0° \leq \varphi \leq 90°$.

The sequence of inclination angles are chosen as $0°$, $15°$, $30°$, $45°$, $60°$, $75°$ and $90°$. The values of d_{EUV} for these seven clouds are listed in Table 3, from which we can see that the ionizing penetration depth decreases with φ, and is very shallow, with values $\ll 1$. As a result, all of these clouds are in the RDI-induced shock-dominated regime and triggered collapse is expected.

3.2.1 Morphological variation with φ

It is found that the evolutionary sequences of the seven clouds are qualitatively similar to that with $\varphi = 45°$, i.e. the formation of a condensed layer on the star-facing surface of the cloud and highly condensed core(s) near the apex, although the final morphologies themselves depend on the initial inclination angle of the cloud. As the general evolution is so similar, they are not discussed individually, but with focus on comparison of the differences in their final morphologies and the physical properties of any high-density core(s). In Fig. 6, the final snapshots of column density of cloud G1200(5) from six different simulations with $\varphi = 0°$, $15°$, $30°$, $60°$, $75°$ and $90°$ are presented. The equivalent for $\varphi = 45°$ can be found in Fig. 3.

When the inclination angle φ is small ($\leq 30°$), $x_a \approx x_{max}$, the EUV radiation mainly illuminates the surface of the front semi-ellipsoid. The effect of the RDI is to drive a pseudo-plane-parallel shock propagating into the cloud, and the prolate cloud evolves to a filamentary structure with a condensed surface layer on the star side and highly condensed core(s) at the apex (when $\varphi \neq 0°$) or at either the apex or the two ends (when $\varphi = 0°$). For the latter case, the evolution has been analysed in detail by Kinnear et al. (2014).

When $45° \leq \varphi < 90°$, the EUV radiation illuminates not only the surface of the front semi-ellipsoid, but also the top part of back semi-elliptical surface, so that the shock induced by RDI creates a condensed and curved surface layer with the apex as a convergence point of two compressed curving surface layers, those surfaces on opposing sides of the apex. The region around the apex is also the
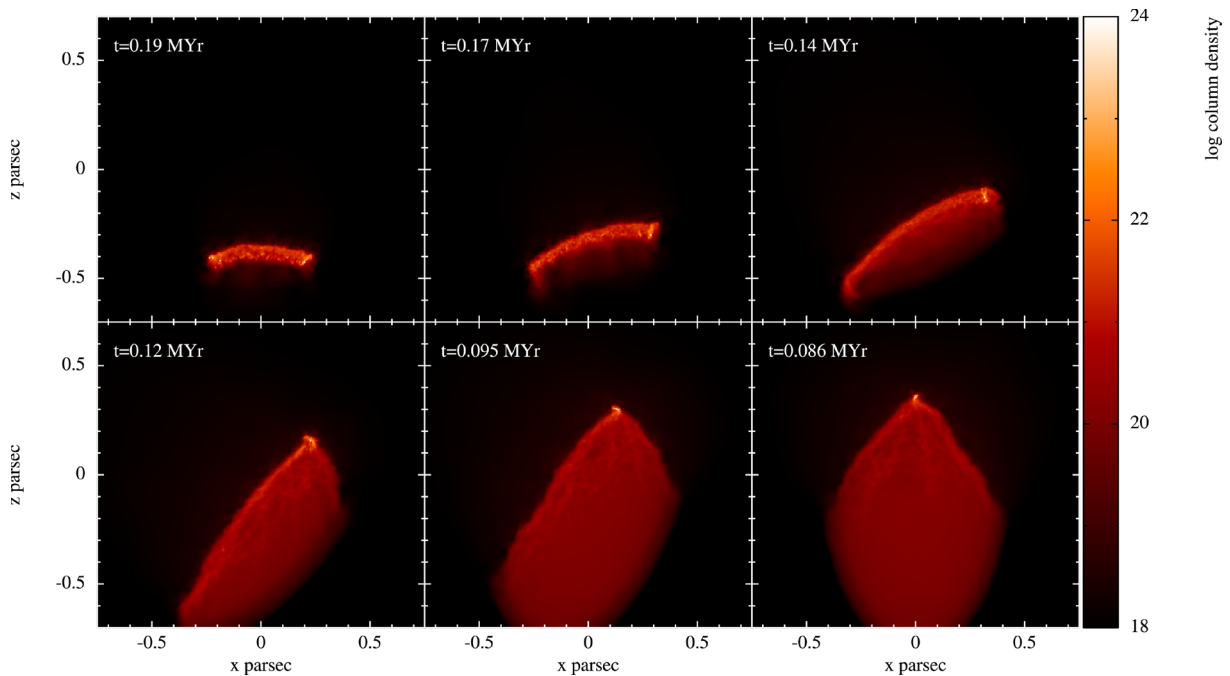
Figure 6. The final snapshot of the column density from six simulations of G1200(5) with different initial inclination angles; left to right then up to bottom are per $0°$, $15°$, $30°$, $60°$, $75°$ and $90°$.
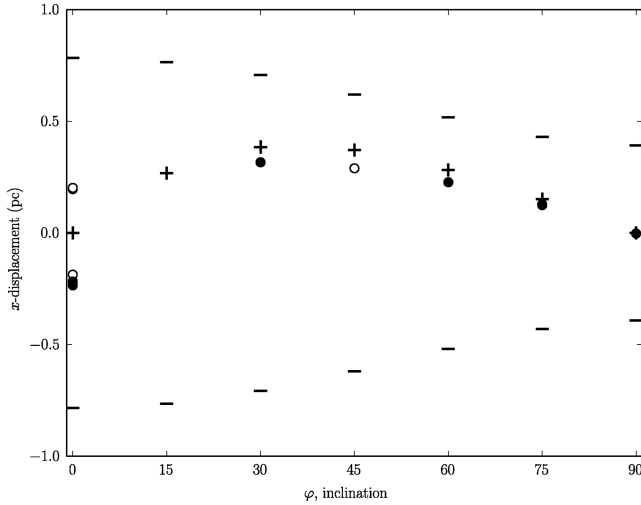
Figure 7. The *x*-displacement of the cores formed in G1200(5) with different initial inclination angles. The short '−' indicates x_{max}, '+' x_p, '○' for the cores with $10^8 \le n_{peak} \le 10^{12}$ cm^{-3}, and '●' for the extremely high density cores with $n_{peak} > 10^{12}$ cm^{-3}.

Figure 8. The evolution of maximum density of the core(s) in the cloud G1200(5) with different initial inclination angles.

site for the formation of high-density core(s). These clouds evolve to asymmetrical BRCs of different morphologies. The morphological sequence is similar to that of the cloud with $\varphi = 45°$, as shown in Fig. 3. Comparing the three final morphologies of the simulations at 45°, 60° and 75° in Figs 3 and 6, we can see that as the inclination angle increases, the final structure of the asymmetrical BRC becomes increasingly extended both in the head and tail. This is because, as the effective EUV illumination area decreases as described in equation (4), the total volume of the cloud affected by the RDI-induced shock becomes smaller. Consequently the original prolate shape of the cloud is less distorted.

When $\varphi = 90°$, the cloud G1200(5) develops into a symmetrical type B/C BRC but having a wide tail structure, with the widest part defined by the initial semiminor axis. The morphology developed is different from that of standard type B/C BRC structure, which has a much narrower width in its tail, if one assumes that the progenitor cloud was initially spherical (Lefloch & Lazareff 1994; Kessel-Deynet & Burkert 2003; Miao et al. 2006, 2009). Observations have also reported several type B/C BRCs with wide tail morphological structures, e.g. SFO74 (Thompson et al. 2004; Kusune et al. 2015).

In summary, a variety of non-standard morphological structures can be obtained by changing the inclination of cloud G1200(5). At low inclination, linear fragment-core structures form, at middle inclinations, asymmetric type B and C structures, and approaching 90° inclinations these return to symmetrical type B and C structures.

3.2.2 The location of high-density cores

Fig. 7 illustrates the distribution of the *x*-displacements of condensed cores formed in the seven simulations of different initial inclination angle φ. A point to note is that, where cores form in very close proximity, their positions cannot be distinguished on the scale used, regardless of the size choice of the marker. It can be seen that when $\varphi > 0°$, core(s) always form at the side of positive *x*-axis and the change of the *x*-displacement with φ follows the trend of x_p with φ. This illustrates an extremely high preference for high-density core(s) to form around the apex x_p in each simulation.
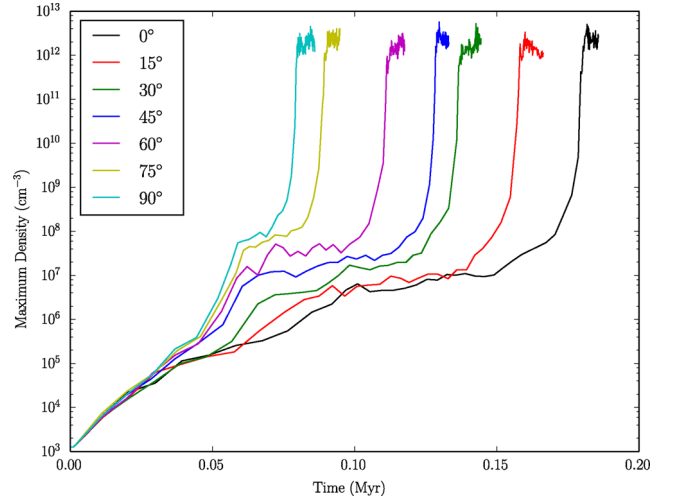
3.2.3 The early triggered core masses and formation time-scales

In order to examine the effect of varying inclination angle on the core properties of RDI-triggered high-density core formation, we investigate the angle dependence of the core formation time and the accumulated core mass. Fig. 8 shows the evolution of the maximum density in the seven simulations with different inclination angles. In general, the evolution of n_{max} in each simulation passes through three different phases: quasi-linear, quasi-stable and steeply rising, although the time of each phase varies with inclination angle φ. These phases may correspond to the different stages of RDI-triggered high-density core formation. Beginning with initial compression by an RDI-induced shock, mass accumulates to form the condensed region, which finally collapses to form high-density core(s). The time for a simulation to reach the highest density (high-density core formation) decreases with inclination angle, from 0.19 down to 0.086 Myr for simulations with $\varphi = 0°$ and 90°, respectively. This is because the curvature of the EUV radiation illuminated surface around the apex of the prolate cloud increases with φ, this is beneficial for mass accumulating towards a geometric focus underneath the curved surface. This decreases the path length to the focus, and so also the time for accumulating mass around it and triggering gravitational instability of the condensed region. On the other hand, the volume of mass swept by the EUV radiation induced shock decreases with φ, which results in a direct decrease in the amount of available mass to be accreted into the cores formed at the head of the BRC. Therefore we should expect that the total mass of the early triggered cores decreases with φ.

The relation between the total high-density core mass and inclination angle φ is shown in Fig. 9, which reveals that the total high-density ($n \ge 10^6$ cm^{-3}) core mass is about 4.1 M$_\odot$, in simulation of $\varphi = 0$, then decreases with φ, becoming 0.4 M$_\odot$ at $\varphi = 90°$. This is consistent with the above expectation. However the total mass of the extremely high density core(s) ($n > 10^8$ cm^{-3}) doesn't show an obvious similar relation with φ to the mass of high-density core(s).

This may be for several reasons. First, as the simulation is curtailed before the end of all of the dynamic processes, extremely high density cores may be on the cusp of formation, but have not yet had the opportunity. Secondly, a large degree of random variation is expected with such gravitational-instability-based collapse.
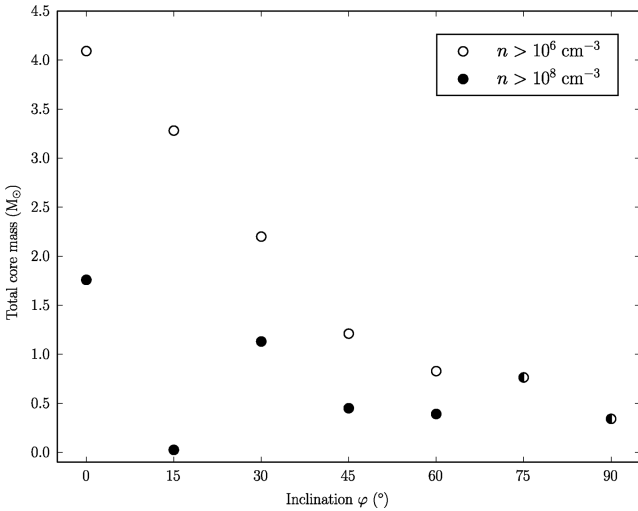
Figure 9. The variation of the total core mass of the cloud G1200(5) over different initial inclination angles. The symbols and their represented properties of cores are shown in the legend box.

Accumulating mass in compact high-density regions can be fairly consistent, but the collapse of these regions or parts of these regions to extremely high densities through gravitational instability is chaotic and varies strongly with the exact configuration of the dynamics.

From the above result, it is understood that as a cloud is rotated from $\varphi = 0°$ to $90°$, the morphology of the cloud varies from fragment-core filamentary structures to varied asymmetrical BRCs, then to standard symmetrical BRCs as φ approaches $90°$. At high

φ, RDI-triggered star formation occurs earlier with lower masses at high densities. However, for the sampling performed, such pattern is not obvious for the extremely high density core formation, which appears to be chaotic. Next we look at the effect of the initial shape of an inclined prolate cloud on its final morphological structure and the properties of the early triggered cores.

3.3 Evolution of G1200 series with $1.0 \leq \gamma \leq 8.0$

The initial shape of the clouds investigated here is defined by the ratio of the major- to minor axis which are in the range of $1.0 \leq \gamma \leq 8.0$. When the initial density and total mass are constants, the major axis changes with γ. The inclination angle is kept at $45°$. The ionization radiation penetration depth ranges from 0.225 to 0.320 per cent as listed in Table 2.

3.3.1 Morphology of final structures

The dynamical evolution of these clouds is also qualitatively similar to that discussed in Section 3.1. We focus on the analysis of the effect of the initial shape of a cloud on the final morphology, the location(s) of the condensed core(s) and the total core masses. Fig. 10 presents six simulation result of cloud G1200 with different initial major- to minor axis ratio $\gamma = 1.0, 1.5, 2.0, 2.5, 3.0, 5.0$, selected from simulation results for 19 different initial clouds, described in Table 2. With increasing γ, the final morphology changes from a standard (symmetrical) type A ($\gamma = 1.0$), to an asymmetric type A BRC ($\gamma = 1.5$), then to an asymmetric type B BRC ($\gamma = 2.0$), next to evolve to an asymmetrical type C BRC ($\gamma = 2.5$). With further increase ($\gamma \geq 3.0$) only a filamentary structure can form.
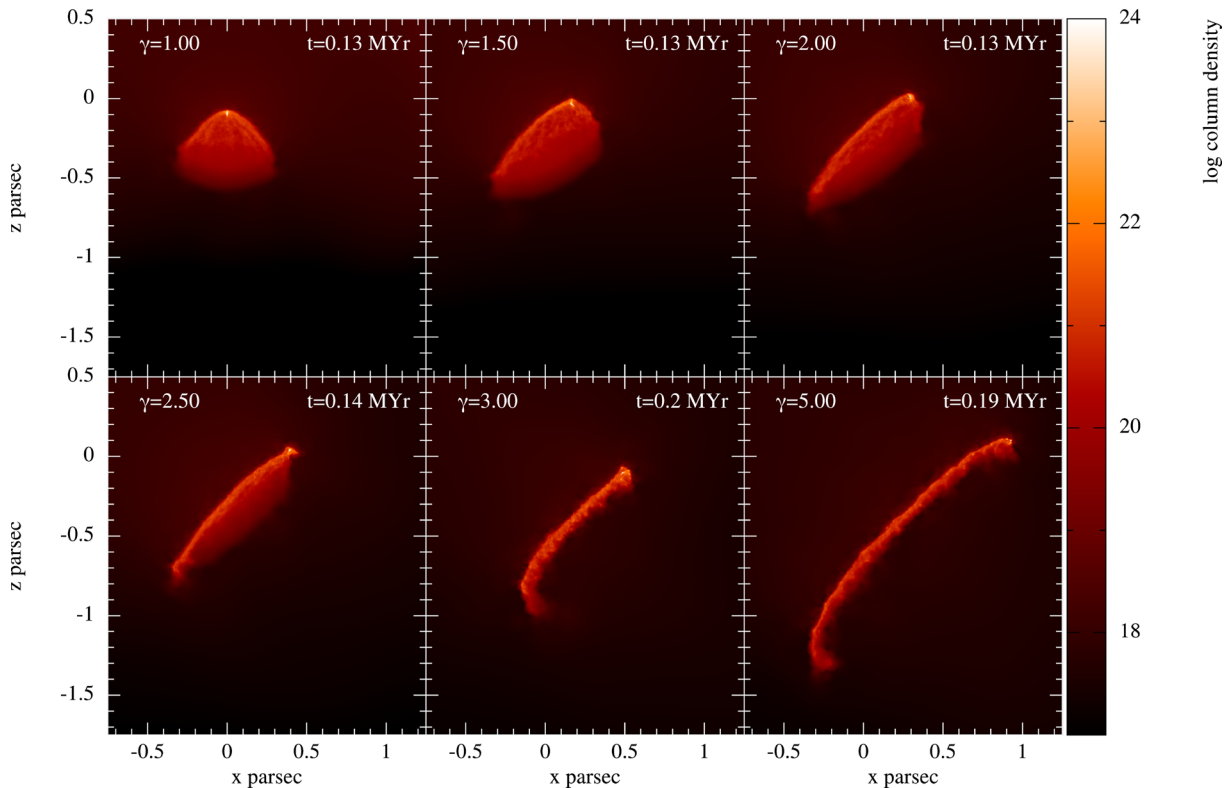

Figure 10. The final snapshots of the column density from six simulations of G1200 with γ equal to the values shown in the top-left corner of each panel. The inclination angle is $45°$ for all of the initial clouds.
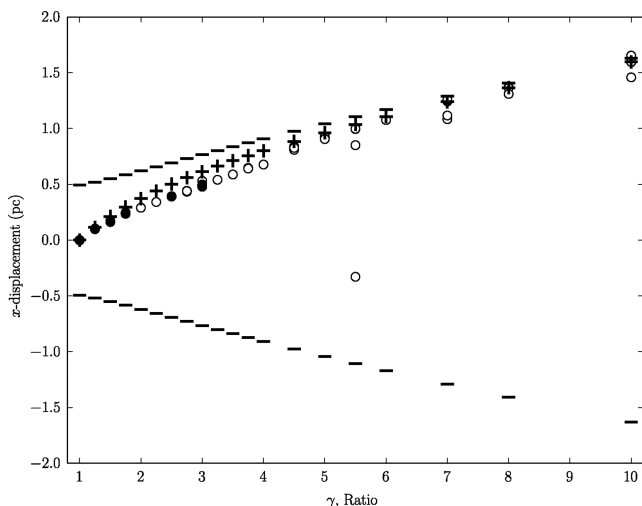
Figure 11. The x-displacement of condensed core in G1200 series with an inclination of $\varphi = 45°$ for varied γ. The short '$-$' indicates x_{max}, '$+$' x_p, '$\circ$' for the cores with $10^8 \leq n_{peak} \leq 10^{12}$ cm^{-3}, and '$\bullet$' for the extremely high density cores with $n_{peak} > 10^{12}$ cm^{-3}.

In these six simulations, high-density cores form at the head of the structure except in the case of $\gamma = 2.5$, where the highly condensed core is embedded in the small 'nose' structure just outside the head. It is interesting to notice that the morphological structure of SFO46 (CG1) from observations (Harju et al. 1990; Haikala, Mäkelä & Väisänen 2010; Mäkelä & Haikala 2013) bears a similar feature to that of $\gamma = 2.5$. We leave the discussion for the formation mechanism of this morphology to the Section 3.4, where we present and analyse more results of various kinds of morphological structures. It is also emphasized that we don't intend to compare the detailed physical structures between simulation and observation on SFO46 in this paper, but only to point out the link between the interesting features from these simulations to such observations. Detailed comparison of physical properties requires further simulations, and will be addressed in a subsequent paper.

3.3.2 Displacement of the high-density cores

Fig. 11 displays the x-displacement of condensed core(s) with changing geometry, based on the simulation results of 19 clouds with different γ.

With increasing γ, x_p moves further in the $+x$-direction. This pattern is displayed in the same form for the condensed cores. A very clear trend of the core formation occurring at or around the apex for all ratios is exhibited.

3.3.3 The total core mass

The trend of total mass of both the high-density core(s) (open circles) and extremely high density cores (filled black circles) is a decrease with γ. This is illustrated in Fig. 12. The total mass of high-density cores has an approximate pattern of maximum mass of 2.0 M$_\odot$ at $\gamma \approx 2.25$ (with an outlier as high as almost 3.0 M$_\odot$ at $\gamma = 2.75$) and a minimum of 0.6 M$_\odot$ at $\gamma = 8$ (with an unusually low value of only around 0.2 M$_\odot$ for $\gamma = 6.0$). Clouds with lower ellipticity appear to have a higher probability of collecting greater mass in the final cores. This can be expected as the mass per unit length along the major axis decreases with γ. As a result, the amount of mass able to collapse towards the apex region decreases, which
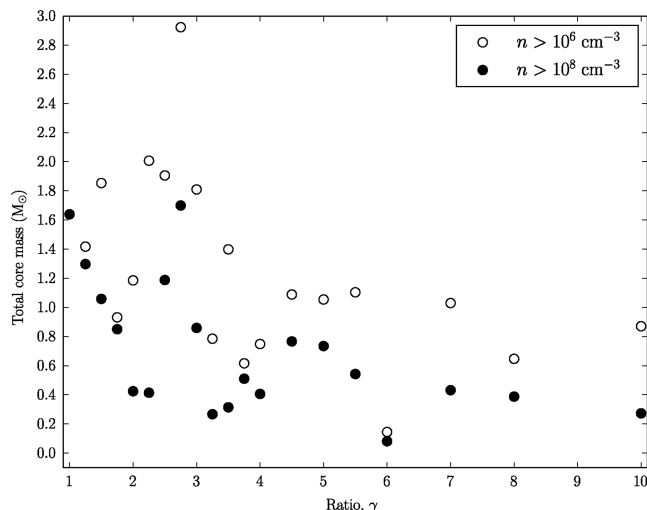

Figure 12. Total mass of condensed cores in cloud G1200 series at an inclination of 45° for varied axial ratio γ.

is similar to the case when $\varphi = 0°$ (Kinnear et al. 2014). When $\varphi \neq 0°$, due to the wide range of variation in the final morphologies of the clouds, the amplitude of the fluctuation is similarly increased.

From the same figure, we can see the mass of extremely condensed cores (filled black circles) in a cloud also decreases with γ in a similar way as the high-density core. The mass of these cores corresponds to the precursor mass for possible protostars forming later in the evolution of the cloud, having a maximum of ≈ 1.6 and a minimum of ≈ 0.2 M$_\odot$.

3.4 Morphological evolution of clouds of different initial density and under different ionizing flux

After the investigation of the effects of both initial shape and inclination angle of a prolate cloud on its RDI-triggered dynamical evolution, we now explore the consequences of changing the initial density of a cloud and the ionizing radiation flux in the morphological development of a cloud of mass 30 M$_\odot$. This is essentially to examine the consistency of the d_{EUV} parameter in characterizing a wider variety of cloud parameters.

A sequence of eight different initial densities are chosen as 100, 200, 400, 600, 700, 800, 1000 and 1200 cm^{-3}. Two different ionization fluxes of $F_1 = 1.0 \times 10^9$ cm^{-2} s^{-1} and $F_2 = 2.0 \times 10^9$ cm^{-2} s^{-1} are applied for a total of 16 simulations. An inclination angle of 60° and $\gamma = 2.0$ is used for all cases. This is as a result of the simulation of G1200(5) exhibiting the formation of the 'nose' structure in the vicinity of these geometries. As such, we can also expect to get some clue of how the 'nose' structure is developed and changes with the initial properties of a cloud in this set of simulations. The corresponding parameters of the clouds are listed in Table 4. It is seen that the change in EUV radiation penetration depth over the initial density ($100 \leq n \leq 1200$ cm^{-3}) is almost two orders of magnitude, a much more dramatic variance than from changing γ or φ.

3.4.1 An overview of the final morphological structures

Fig. 13 displays the final snapshots of the column density of the eight simulations with ionization flux of F_1. The morphology of the final structure of a cloud changes from an asymmetrical type C BRC to a filamentary structure and then to an irregular structure, as

Table 4. Parameters of molecular clouds of mass 30 M$_\odot$, an inclination angle $\varphi = 60°$, $\gamma = 2$ and $a_{crit} = 0.079$ (pc). From left to right, columns are the cloud index, initial number density, the major axis and d_{EUV} defined by equation (8), with different ionization flux F_1 and F_2 being 1.0×10^9 and 2.0×10^9 cm^{-2} s^{-1}, respectively.

Index	n (cm^{-3})	a (pc)	$d_{EUV}(F_1)$ (per cent)	$d_{EUV}(F_2)$ (per cent)
G100	100	1.797	11.779	23.558
G200	200	1.427	3.708	7.416
G400	400	1.132	1.17	2.34
G600	600	0.989	0.594	1.188
G700	700	0.940	0.460	0.920
G800	800	0.899	0.368	0.736
G1000	1000	0.834	0.254	0.508
G1200	1200	0.784	0.187	0.374

the initial density is decreased from 1200 to 100 cm^{-3}, which leads to an increase of d_{EUV} from 0.187 to 11.779 per cent.

As shown in the top row panels, an asymmetrical type C BRC is developed in G1200, G1000, G800 and G700, with d_{EUV} of 0.187, 0.254, 0.368 and 0.460 per cent, respectively. Although they all bear an asymmetric type C BRC morphology, the minor axis becomes narrower with increasing d_{EUV}, which results in more cloud material being photoevaporated from their star-facing surfaces. When the initial density $n = 600$ cm^{-3} ($d_{EUV} = 0.594$ per cent), the prolate cloud evolves into a filamentary structure, as shown in the first panel in the bottom row of Fig. 13. Clouds of initial densities of 400, 200 and 100 cm^{-3} ($d_{EUV} = 1.17$, 3.708 and 11.779 per cent, respectively) are all seen to form irregular structures.

The final morphological structures from the simulations using doubled ionization flux F_2 are presented in Fig. 14. Similar morphological structure sequences to those seen in Fig. 13 are observed. An asymmetrical type C BRC is formed from G1200, G1000 and G800, a filamentary structure from G700, and irregular structures in G600, G400, G200 and G100. The only difference is that the morphological transition point shifts to a cloud of higher initial density compared to the F_1 simulations.

The first transition from type C BRC to filamentary morphology occurs around G600(F_1) and G700(F_2), and the second transition from filamentary to irregular morphology is around G400(F_1) and G600(F_2). These appear to correspond to similar d_{EUV} in each case, for both fluxes. The former transition occurs at $d_{EUV} \approx 0.8$ and the latter at $d_{EUV} \approx 1.1$. This indicates that d_{EUV} remains a characteristic parameter for the dynamical evolution of a cloud for the parameter space so far investigated.

Figs 15 and 16 present the core formation time and the total mass of the RDI-triggered condensed cores versus the initial density of the clouds of the above two groups of simulated clouds, with black lines for F_1 group and red for F_2. It is shown that the core formation time in both group clouds decreases with the initial density of a cloud. This is because of the stronger initial gravitational bonding in the high-density cloud. For the same reason, the total mass of the condensed cores follow an increasing trend with the initial density of the cloud. However the effect of the strength of the EUV radiation flux on the time-scales and masses of triggered core formation versus initial density is twofold. When the initial density is below 600 cm^{-3} the clouds illuminated by the higher flux (F_2) take a longer time to form condensed cores, and collect slightly more mass in their condensed cores than in the clouds illuminated by the lower flux (F_1). This trend is reversed when the initial density is
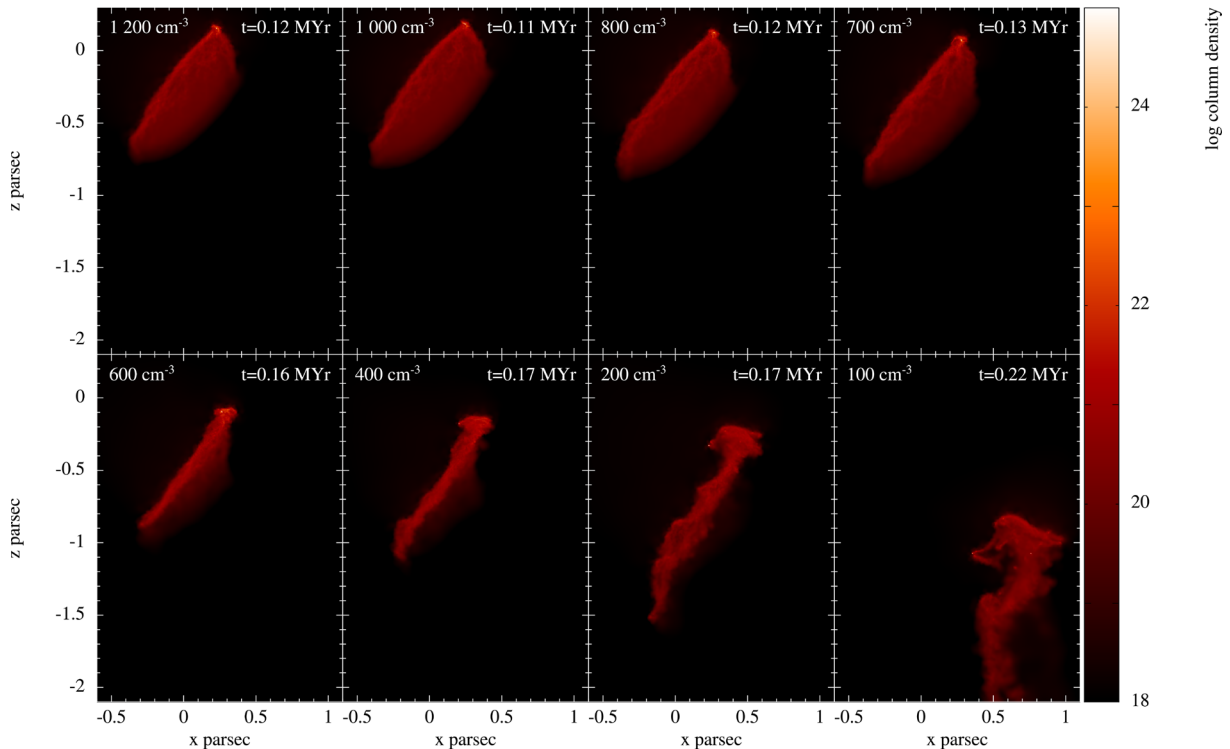
Figure 13. The final snapshot of the column density of clouds of initial mass of 30 M$_\odot$, $\gamma = 2.0$ and $\varphi = 60°$ but different initial densities as shown in the top-left corner of each panel. The ionization flux $= 10^9$ cm^{-2} s^{-1}.
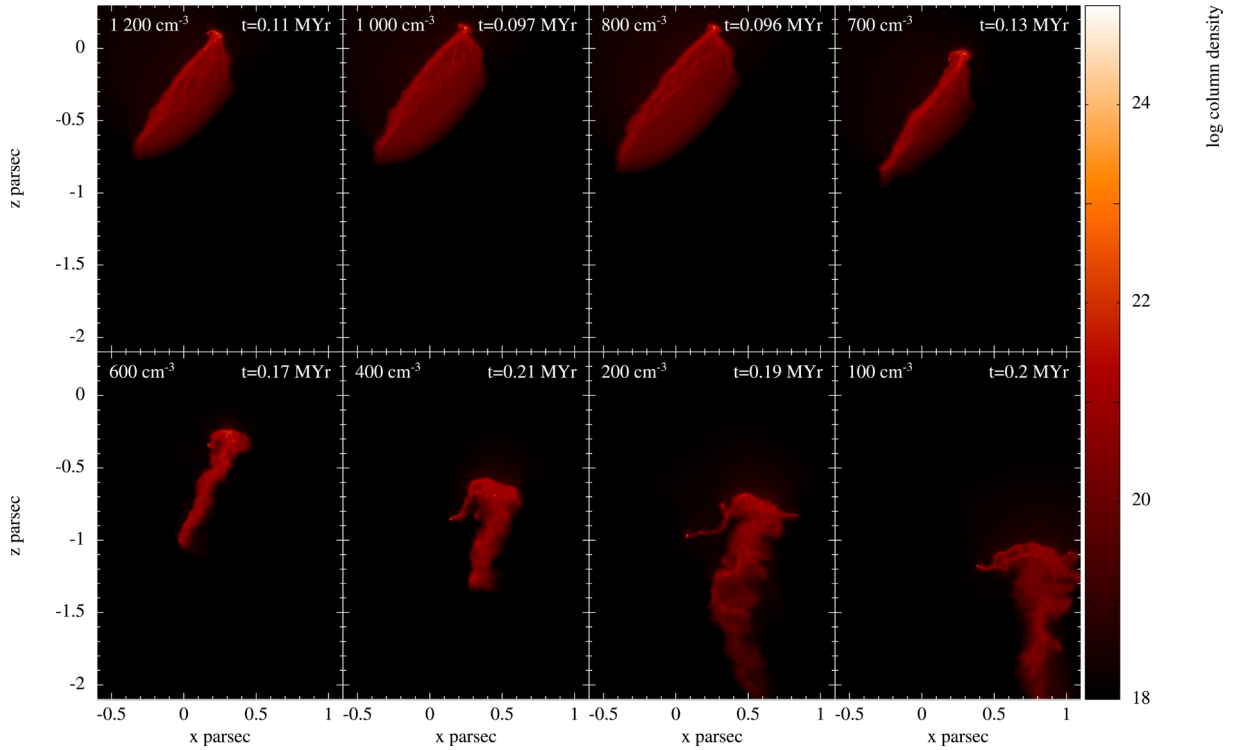
Figure 14. The final snapshot of the column density of the same eight clouds as in Fig. 13 (initial mass of 30 $M_\odot$, $\gamma = 2.0$ and $\varphi = 60°$) but with increased incident flux of 2×10^9 cm^{-2} s^{-1}.
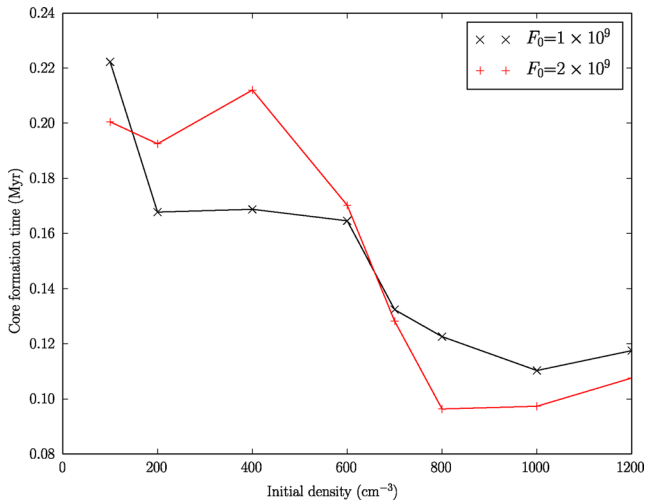

Figure 15. The core formation time of the F_1 and F_2 group clouds versus their initial densities.

Figure 16. The total mass of the cores formed in F_1 and F_2 group clouds versus their initial densities.

higher than 600 cm^{-3}, i.e. clouds illuminated by higher flux take less time to form condensed core and collect less mass into their condensed cores than the clouds illuminated by lower flux.

Overall, the information delivered in the above two figures suggests that the effectiveness of RDI-triggered star formation, measured as a combination of formation speed and masses of the early cores, is much higher (shorter core formation time and higher total core mass) in molecular clouds of shorter d_{EUV} (corresponding to higher initial density) in both F_1 and F_2 group clouds.

From the above two sets of simulations, we can see that when $d_{EUV} \geq 1.0$ per cent, the deep penetration of the EUV radiation into the cloud causes irregular structure formation. A closer look
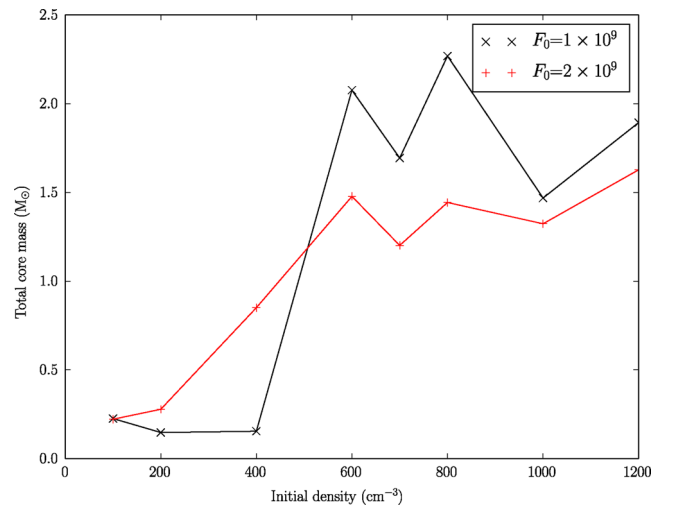
at the above two morphological variation sequences tells that with increasing d_{EUV}, the tiny 'nose' structure around the apex of the asymmetrical type C BRC gradually grows and becomes an irregular 'horse-head' structure. In order to understand how the 'nose' and 'horse-head' structures form, we further investigate the evolutionary process of one of the above clouds, which presents a clear horse-head-like morphology.

3.4.2 Growing from 'nose' to 'horse-head' structure

We chose the cloud G400(F_2) to analyse its evolutionary process due to its formation of a particularly distinctive 'horse-head'
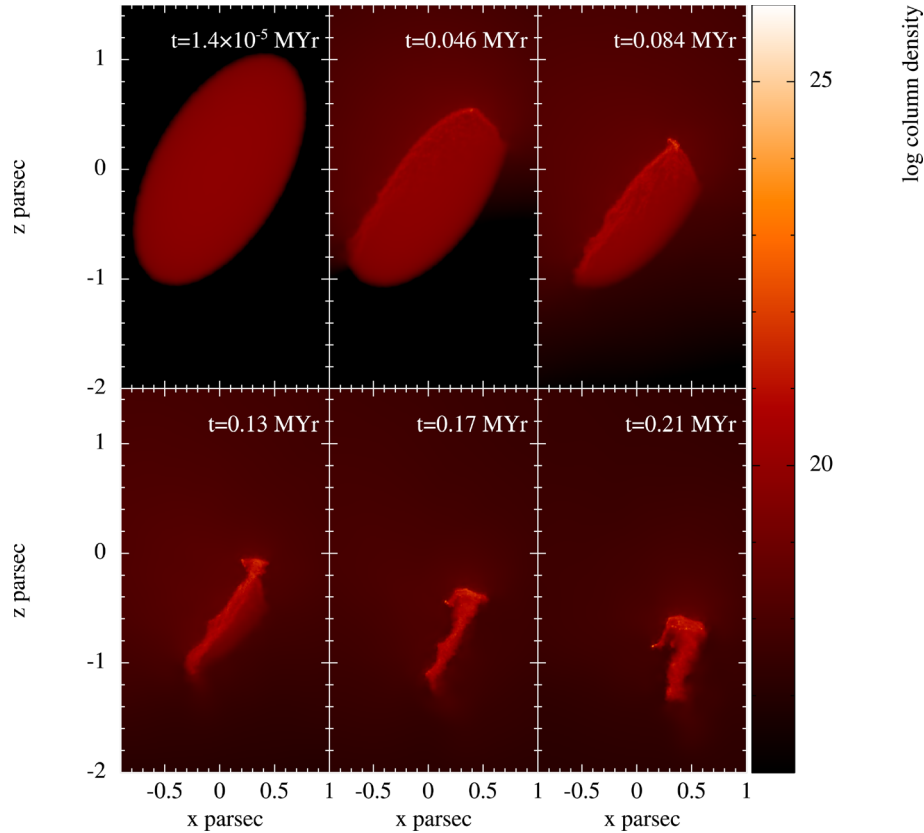
Figure 17. The column density evolution of a cloud G400(F_2), with an inclination angle of 60°.

structure. Fig. 17 describes a six-snapshot column density evolutionary sequence of cloud G400(F_2), which shows a growing process from a small 'nose' to a 'horse-head' morphological structure. The corresponding RDI-induced shock velocity profiles for each of the snapshots are plotted in Fig. 18, which reveals the kinematic mechanism for the morphology formation in G400(F_2).

From Fig. 17, we can see that a shocked layer forms at $t = 0.046$ Myr, which surrounds most of the surface of the front semi-ellipsoid and a small part of the top surface of the back semi-ellipsoid. The maximum magnitude of the shock velocity $v_s = 12$ km s^{-1}, calculated as the peak velocity of non-ionized gas within the condensed shock front. Most of the shocked layer surrounding the front semi-ellipsoid propagates into the cloud smoothly towards $(+x, -z)$ direction. Very close to the apex, the shock velocity of the front semi-ellipsoid is towards the direction of $(x, -z)$, and that of the back semi-ellipsoid is $(-x, -z)$, the gas material from the two sides of the apex converge beneath the apex to make a small 'nose' structure at $t = 0.084$ Myr, as shown in the top-right panels of Figs 17 and 18.

While a small 'nose' structure forms at the point of $(x, z) \approx$ (0.2, 0.2) pc and with $v_x \approx 0$, below the nose structure, the RDI-induced shock keeps pushing the surface layer of the front semi-ellipsoid moves towards the $(+x, -z)$ direction at the shock velocity. This makes the below-nose region of the BRC gradually produce a displacement along x-direction relative to the nose. The nose becomes a short horizontal fragment at $t = 0.13$ Myr, in which the direction of the RDI-induced shock velocity is mainly along z-direction. The short horizontal fragment gradually forms a 'hook' at $t = 0.17$ Myr as shown in the lower-middle panels of Figs 17 and 18. Further propagation of the shocked layer below the hook

towards $(+x, -z)$ direction makes the 'hook' structure grow to look like a 'horse-head' as shown in the last panels in the above two figures. The final 'horse-head' structure bears some resemblance to the well-known horse-head nebula.

It is seen from the above analysis that the appearance of a 'horse-head' morphology in this instance is a consequence of growing a small 'nose' structure. The 'nose' structure forms if the gas around the apex of an ellipsoidal cloud converge beneath that apex due to a strong RDI-induced shock effect, as described above. This requires that the cloud should have a reasonably high inclination angle, i.e. $\varphi > 45°$ in our simulations. However the formation of a 'nose' structure does not necessarily lead to a 'horse-head' structure. For example, a small 'nose' formation is seen from the final morphologies of G700–1200 in the F_1 series and G800–1200 in the F_2 series. Whether the 'nose' can grow into a 'horse-head' also depends on the initial ionization penetration depth, i.e. $d_{EUV} > 1.0$ per cent. The latter is to guarantee a higher enough shock velocity ($v_s \sim \sqrt{\frac{F_{Lyman}}{n}}$)(Bertoldi 1989), which can push the majority of the gas below the nose towards the $(+x, -z)$ direction.

3.5 Development of other irregular morphologies

Further simulations were conducted, to explore if there are other structures which form different irregular morphologies to a 'horse-head' as a consequence of the variation of initial conditions of the cloud and ionization flux. A series of 16 simulations with G400(F_2) of different $\gamma = 2.0, 2.5, 3.0, 3.5$ and $\varphi = 60°, 70°, 80°, 85°$ are conducted. For all 16 clouds, $d_{EUV} > 1.0$ per cent. In this section, we concentrate on the description of the morphological variations,
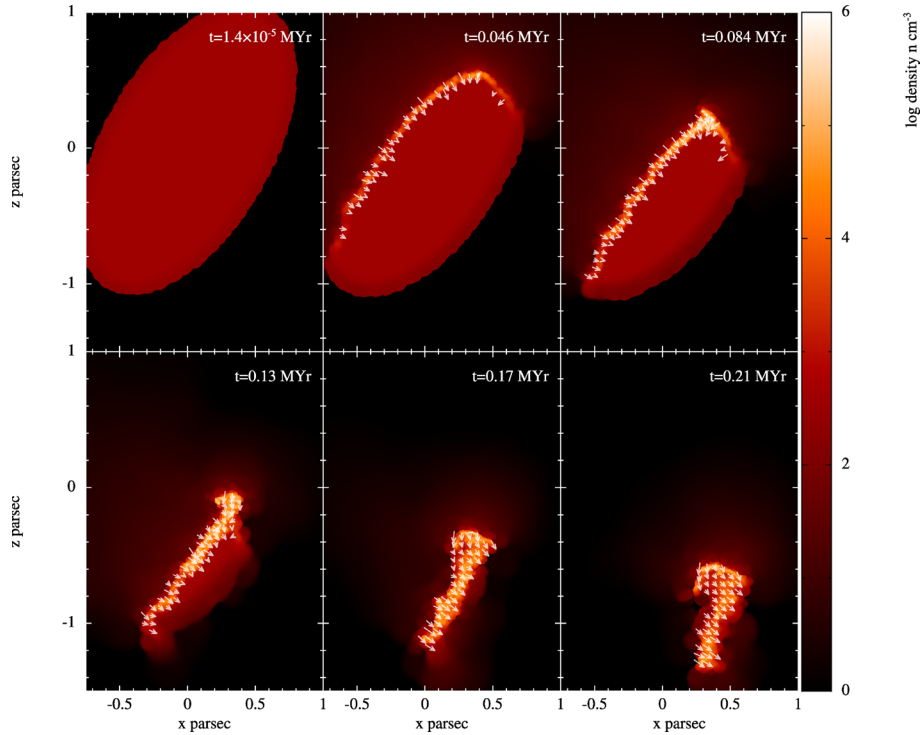
Figure 18. The evolution of the RDI-induced shock velocity of cloud G400(F_2) overlapped in the corresponding cross-section density snapshot. The magnitude of the velocity is between 2 and 12 km s^{-1}.

as the underlying mechanisms appear to be similar, and they are of interest due to their variety rather than exact evolutions.

The first-column panels in Fig. 19 present the final morphologies of G400(F_2) of $\gamma = 2$ and 4 different initial inclination angles, which show that when the initial angle φ increases from 60°, the 'horse-head' in the final structure becomes longer in z-direction. The connection point between the 'horse-head' and the below-horse-head part moves downwards with φ. At 85°, the whole morphology is an 'elephant trunk' like structure. This is because the 'nose' structure formed in the first tens of kyr of the evolution increasingly stretches along the z-axis with increasing φ. The first-row panels in Fig. 19 describe the morphology change of cloud G400(F_2) of inclination angle $\varphi = 60°$ and varied γ. When the initial prolate cloud becomes more elliptical, in addition to a 'horse-head' structure, the RDI-induced shock also triggers linear gravitational instability along the direction of the major axis in some clouds.

The 16 panels in Fig. 19 present 16 different final morphologies which appear in the clouds of the initial (γ, φ) as stated above. We can conclude that the larger the inclination angle, the longer the 'horse-head' sub-structure; and that the more elliptical the cloud initially, the thinner the final morphology is. Although, as in previous instances, their structural details differ across the range of γ.

Through viewing more simulation results obtained using different combination of $(F_{Lyman}, n, \gamma, \varphi)$, we find that the variety of the final morphology is extensive for $d_{EUV} > 1.0$ per cent, although it is impossible to show all of them in this paper.

4 CONCLUSIONS

The results from the simulations conducted show that uniform density prolate clouds at an inclination to a plane-parallel EUV radiation field can evolve to a variety of morphological structures often found

at various H II boundaries. The parameter of EUV radiation penetration depth, d_{EUV}, of a given cloud can be a good indicator as to whether it would evolve to a regular BRC or irregular structures.

The final morphology of the clouds of initial density (1200 cm^{-3}) and ellipticity ($\gamma = 2$), and with $d_{EUV} < 1.0$ per cent changes from a filament to an asymmetrical BRC, then to a symmetrical BRC, as the inclination angle φ increases from 0° to 90°. The core formation time decreases with φ, as the curvature of the EUV radiation illuminated surface increases with φ, which leads to a shorter path-length for mass to converge to the focal point beneath the tip of the BRC. The total core mass of early triggered cores also decreases with φ because less volume of mass available to converge to the cores. Therefore EUV radiation triggered star formation is quicker in high φ prolate clouds, but the total mass of the triggered stars is higher for low φ cloud.

For clouds of fixed initial density (1200 cm^{-3}) and inclination angle ($\varphi = 45°$), as γ increases from 1 to 8, the final morphologies change from a symmetrical to asymmetrical BRC, then to filamentary structure. The total mass of early triggered cores decrease with the increase of γ, due to the decreased mass per unit length causing less effective collection of material by the converging shock.

It is found that the final morphology of a prolate cloud is very sensitive to the initial density. For fixed initial shape ($\gamma = 2.0$) and fixed inclination angle ($\varphi = 60°$), the morphology of a cloud changes from an asymmetric type C BRCs to a filament then to irregular structures, such as a 'horse-head', as the initial density decreases from 1200 to 100 cm^{-3}. Early triggered core masses are found to be higher in regular BRCs (with $d_{EUV} < 1.0$ per cent) than in irregular structures (with $d_{EUV} > 1.0$ per cent).

Based on the above systematic investigation on the evolution of molecular clouds (or clumps) at an H II boundary, we can now suggest a unified formation mechanism for the different morphological structures seen in the published images of a variety of
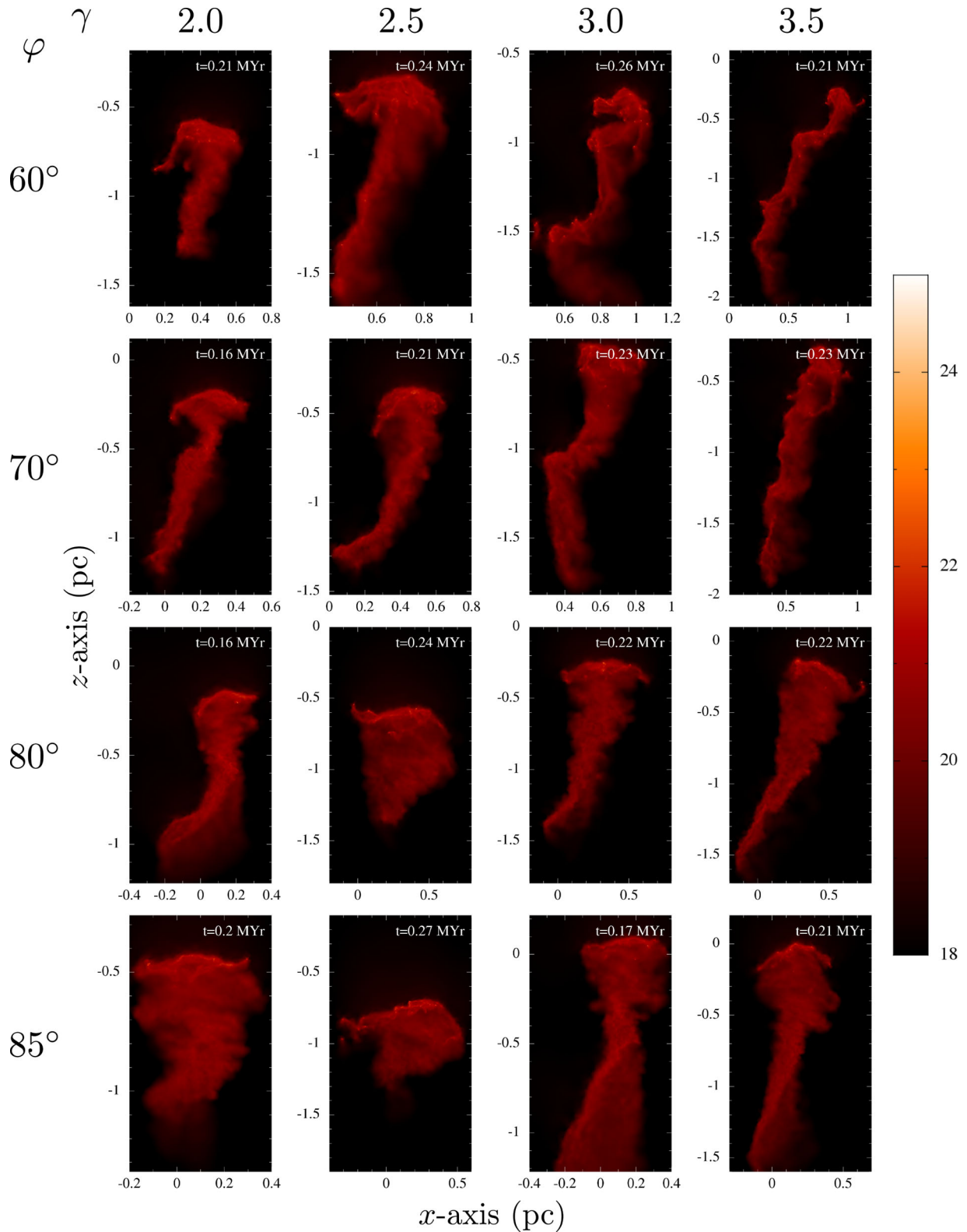
Figure 19. The final morphologies of the clouds G400(F_2) of different initial geometry and inclination angle. The axis scales vary between panels, because of the different initial scale of the major and minor axes for the clouds depicted.

H II regions: giant molecular clouds (GMCs) are clumpy and the numerous clumps are of different shapes, from spherical to highly elliptical, and with their major axes not exhibiting a strong preference for any particular alignment within their environment. When a star or a cluster of stars forms inside a GMC, the interaction between the ionizing radiation with the surrounding molecular clumps of different shapes and orientations creates structures of various morphologies. The spherical and prolate clumps aligned with the

radiation flux form standard type BRCs, the inclined prolate clumps with a shallow ionizing radiation penetration depth form asymmetrical BRCs or an inclined linear structures; the inclined prolate clumps with a deep radiation penetration depth form a variety of irregular structures, the well-known 'horse-head' structure is only one of them.

In our next paper, we are going to investigate the evolution of physical properties of a few observed asymmetrical BRCs and the RDI-triggered star formation inside them.

ACKNOWLEDGEMENTS

REFERENCES

Bastien P., 1983, A&A, 119, 109
Bate M. R., Burkert A., 1997, MNRAS, 288, 1060
Bertoldi F., 1989, ApJ, 346, 735
Bisbas T. G., Wünsch R., Whitworth A. P., Hubber D. A., Walch S., 2011, ApJ, 736, 142
Chauhan N., Pandey A. K., Ogura K., Jose J., Ojha D. K., Samal M. R., Mito H., 2011, MNRAS, 415, 1202
Doty S. D., Everett S. E., Shirley Y. L., Evans N. J., Palotti M. L., 2005, MNRAS, 359, 228
Dyson J. E., Williams D. A., 1997, The Physics of the Interstellar Medium. IoP Publishing, Bristol
Fukuda N., Miao J., Sugitani K., Kawahara K., Watanabe M., Nakano M., Pickles A. J., 2013, ApJ, 773, 132
Gammie C. F., Lin Y.-T., Stone J. M., Ostriker E. C., 2003, ApJ, 592, 203
Gholipour M., Nejad-Asghar M., 2013, MNRAS, 429, 3166
Gong H., Ostriker E. C., 2011, ApJ, 729, 120
Gritschneder M., Naab T., Walch S., Burkert A., Heitsch F., 2009, ApJ, 694, L26
Habing H. J., 1968, Bull. Astron. Inst. Neth., 19, 421
Haikala L. K., Mäkelä M. M., Väisänen P., 2010, A&A, 522, A106
Harju J., Sahu M., Henkel C., Wilson T. L., Sahu K. C., Pottasch S. R., 1990, A&A, 233, 197
Haworth T. J., Harries T. J., 2012, MNRAS, 420, 562
Karr J. L., Noriega-Crespo A., Martin P. G., 2005, AJ, 129, 954
Kessel-Deynet O., Burkert A., 2000, MNRAS, 315, 713
Kessel-Deynet O., Burkert A., 2003, MNRAS, 338, 545
Kinnear T. M., Miao J., White G. J., Goodwin S., 2014, MNRAS, 444, 1221
Kusune T. et al., 2015, ApJ, 798, 60
Lefloch B., Lazareff B., 1994, A&A, 289, 559
Mäkelä M. M., Haikala L. K., 2013, A&A, 550, A83
Miao J., White G. J., Nelson R., Thompson M., Morgan L., 2006, MNRAS, 369, 143
Miao J., White G. J., Thompson M. A., Nelson R. P., 2009, ApJ, 692, 382
Miao J., Sugitani K., White G. J., Nelson R. P., 2010, ApJ, 717, 658
Morgan L. K., Thompson M. A., Urquhart J. S., White G. J., Miao J., 2004, A&A, 426, 535
Nelson R. P., Langer W. D., 1999, ApJ, 524, 923
Nelson R. P., Papaloizou J. C. B., 1993, MNRAS, 265, 905
Oort J. H., Spitzer L., Jr, 1955, ApJ, 121, 6
Osterbrock D. E., 1957, ApJ, 125, 622
Panwar N., Chen W. P., Pandey A. K., Samal M. R., Ogura K., Ojha D. K., Jose J., Bhatt B. C., 2014, MNRAS, 443, 1614
Price D. J., 2007, Publ. Astron. Soc. Aust., 24, 159
Rathborne J. M., Johnson A. M., Jackson J. M., Shah R. Y., Simon R., 2009, ApJS, 182, 131
Sicilia-Aguilar A., Roccatagliata V., Getman K., Henning T., Merín B., Eiroa C., Rivière-Marichalar P., Currie T., 2014, A&A, 562, A131
Springel V., 2005, MNRAS, 364, 1105
Sugitani K., Ogura K., 1994, ApJS, 92, 163
Sugitani K., Fukui Y., Ogura K., 1991, ApJS, 77, 59
Thompson M. A., Urquhart J. S., White G. J., 2004, A&A, 415, 627
Tremblin P., Audit E., Minier V., Schneider N., 2012, A&A, 538, A31
Urquhart J. S., Thompson M. A., Morgan L. K., White G. J., 2006, A&A, 450, 625

This paper has been typeset from a TEX/LATEX file prepared by the author.